

# Analytical model of the laser ablation mechanism of Lithium-Ion battery coatings

Benjamin Schmieder<sup>\*a</sup>

<sup>a</sup>Manz AG, Steigaeckerstrasse 5, 72768 Reutlingen, Germany

## ABSTRACT

In Lithium-Ion battery production many different active material coatings are used to serve the individual needs of the final product. Furthermore laser processing becomes the method of choice in the production to allow a maximum degree of freedom and reduce tooling costs. The used electrode coatings and its different components highly influence the laser process and its results in terms of quality and efficiency. To achieve a better understanding of the ablation mechanism high speed video recording was used to allow a more detailed observation of the cutting and ablation mechanism, respectively. Based on these insights an analytical model was created and verified by time resolved shadowgraph imaging and experimental determined laser ablation thresholds.

**Keywords:** Li-Ion battery, laser cutting, laser ablation, consumer electronics

## 1. INTRODUCTION

Especially in consumer electronics the energy density of batteries is an important factor. On one side due to the fact that space in devices like smart phones is limited. On the other side these devices contain energy demanding components. Additionally in order to prevent lithium plating and subsequent dendrite growth the anode should overhang the cathode. This leads to extra dead volume ( $V_d$ ) that does not support the energy density of the cell. In addition to this inherent dead volume and tolerances like cutting accuracy (footprint accuracy) and staking or winding tolerances the geometry of the laser cut electrode edges accrue to the dead volume. Figure 1 shows a schematic view of a laser cut electrode edge.

\*bschmieder@manz.com; phone +49 (0)7121 554; mobile +49 (0)151 23478892; manz.com

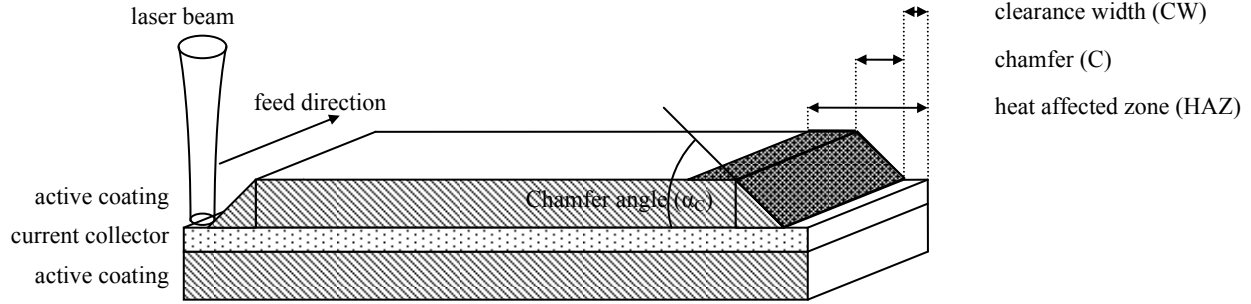


Figure 1: Schematic cross section view of a laser cut electrode.

Depending on the aspect ratio of the cell (i.e. number of electrodes per cell ( $n$ ) / cell footprint ( $A_{\text{cell}}$ )) the effect of this edge geometry caused by laser cutting gets more dominant for cells with smaller footprint. This is usually the case for cells that are used in consumer electronics compared to their automotive industry counterparts. Figure 2 illustrates the setup of a typical half cell and Equation (1) and (2) describe the amount of dead volume of a half Cell.  $h_{\text{halfcell}}$  is the total thickness of the half cell,  $a_c$  and  $b_c$  describe the width and length of the cathode excluding  $CW_c$  and  $C_c$ ,  $a_a$  and  $b_a$  represent the width and length of the anode including  $CW_a$  and  $C_a$ .

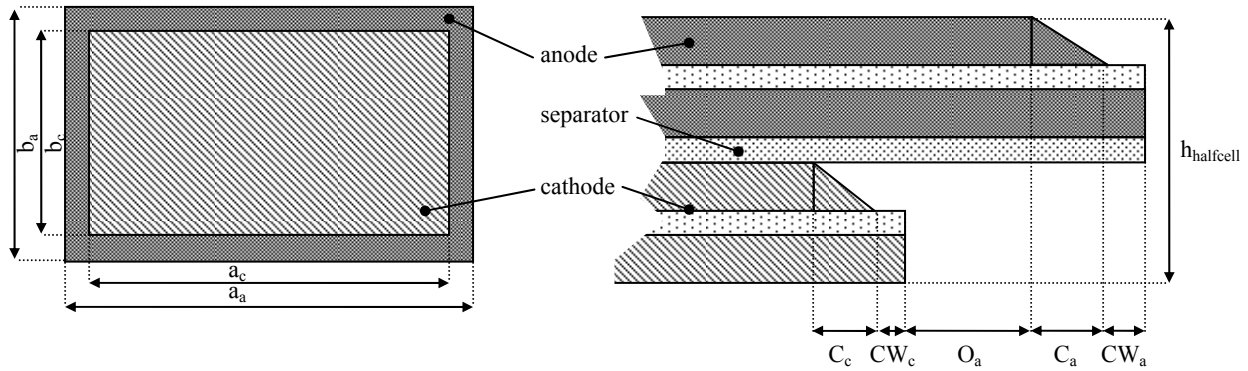


Figure 2: Schematic view of a half cell setup with the typical anode overhang and a non oversized separator.

$$Vd_{\text{halfcell}} = (A_{\text{total}_a} - A_{\text{active}_c}) \cdot (h_{\text{halfcell}}) \quad (1)$$

$$Vd_{\text{halfcell}} = (a_a \cdot b_a - (a_a - 2(C_c \cdot CW_c \cdot O_a)) \cdot (b_a - 2(C_c \cdot CW_c \cdot O_a))) \cdot (h_{\text{halfcell}}) \quad (2)$$

The following Figure 3 shows the  $Vd_{halfcell}$  proportion of a square shaped ( $a = b$ ) half cell calculated by (2).

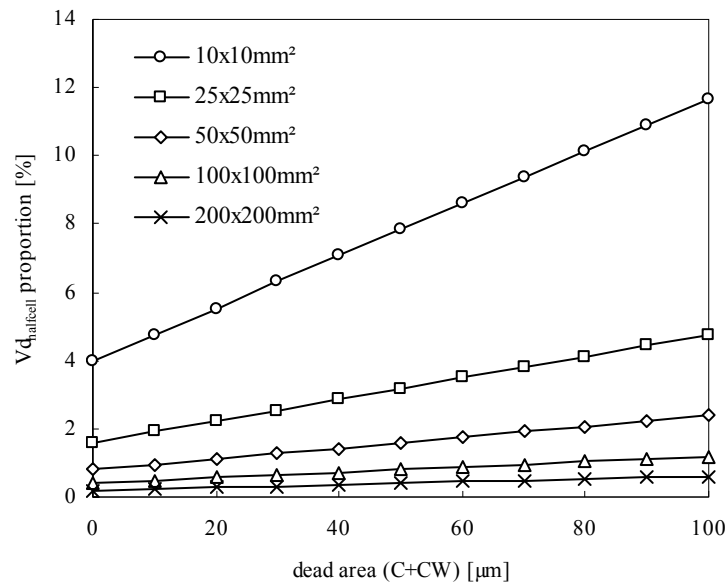


Figure 3: Dead volume proportion of a half cell in dependence of the total cell foot print and the dead area width ( $C+CW$ ).

The anode overhang ( $O_a$ ) is given by electro chemical restrictions like the prevention of edge lithium plating and dendrite growth [1] and the stacking accuracy. For these reasons the anode overhang was fixed to a width of  $100\mu\text{m}$  which is related to practice at the lower end of the achievable production performance.  $O_a$  is the reason for the offset of the five different datasets in Figure 3. For larger formats the loss of utilizable volume compared to the all over volume is fairly small. Starting at a size of  $50\times 50\text{mm}^2$  the effect gets more dominant. At this cell format and a realistic value of  $C+CW = 75\mu\text{m}$  [2] - [4] the loss of active volume amounts 2 percent. Neglecting factors like packaging of the cell, connective tabs and sealing, this equals approximately 2 percent of capacity loss. At a cell format of  $25\times 25\text{mm}^2$  the theoretical capacity loss under the same conditions increases to almost 4 percent. All the calculations made only consider geometrical deviations from an ideal cutting edge and no factors like heat affected zone (HAZ) as the functionality of an electrode is determined foremost by mechanical defects like  $C$  and  $CW$  [5].

## 2. EXPERIMENTAL

### 2.1. Tested electrode materials

All experiments were performed with the same electrode material. As Anode a standard graphite Material with a copper current collector (CC) was used. The cathode was a NMC ( $\text{Li}(\text{Ni}_{1/3}\text{Mn}_{1/3}\text{Co}_{1/3})\text{O}_2$ ) active material with an aluminium CC. Both electrodes used a PVDF binder ( $(\text{C}_2\text{H}_2\text{F}_2)_n$ ) to achieve cohesion. The mechanical specifications of the electrodes are listed in Table 1.

electrode	Area density [g/cm <sup>2</sup> ]	Total thickness [μm]	CC thickness [μm]	Coating thickness [μm]
Anode	28,1	133	11	61
Cathode	41,3	140	16	62

Table 1: Mechanical specifications of the used electrodes.

The following Table 2 lists the material constants of the anode that have been used for the further calculations.

Material constant	Copper	PVDF	Graphit
Fusion point [K]	1358	435	*
boiling-, sublimation temperatur [K]	3200	660	4098
Enthalpy of fusion [kJ/mol]	13,26	$6,9 \cdot 10^{-4}$	*
Enthalpy of sublimation, evaporation [kJ/mol]	300	*	715
Density [g/cm <sup>3</sup> ]	8,92	1,77	2,16
Specific heat capacity [J/(kg*K)]	385	1040	709
Molar volume [m <sup>3</sup> /mol]	$7,11 \cdot 10^{-6}$	$5,31 \cdot 10^{-6}$	$5,31 \cdot 10^{-6}$
Thermal conductivity [W/(m*K)]	400	0,2	128 / 6
Average particle size [μm]	-	-	10

Table 2: Material constants of the anode components.

## 2.2. Used laser source and parameters

Table 4 lists the parameters and specifications of the beam source that has been used for this investigation.

Manufacturer	Model	Wave length $\lambda$ [nm]	Beam quality $M^2$	Raw beam diameter $D_0$ [mm]	Pulselength $\tau$ [ns]	Maximum pulse energy $E_p$ [mJ]
IPG Lasers	YLP-HP	1055-1065	< 2	< 9	T1: 30	T1: 0.2
	Q-switched				T2: 60	T2: 0.4
	Fibre laser				T3: 120	T3: 1.0
					T4: 240	T4: 1.0

Table 4: Parameters and Specification of the beam source used for all experiments in this study.

Figure 4 shows the measured temporal pulse shaping of operation modes T1-T3.

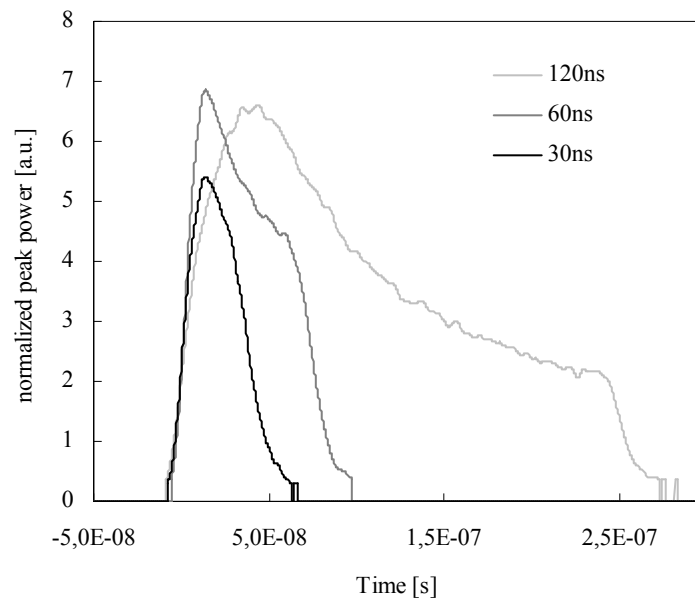


Figure 4: measured temporal pulse shaping of operation modes T1, T2 and T3 at specified  $E_p$ .

## 2.3. High speed video recordings

In order to get a first brief insight, the laser process of cutting Lithium-Ion battery electrodes was visualized by high speed video recording. Figure 5 shows the experimental setup. In order to get a good impression of the process mechanics the high speed camera (HSC) was aligned parallel to the electrode surface plane with a viewing angle perpendicular to the feed direction of the laser beam. In order to get a good temporal resolution of the process at a good picture quality the average power ( $P_L$ ), pulse repetition rate (PRR) and the feed rate were kept fairly low. The used Parameters are listed in Table 5. With this set of parameters a full cut was achieved.

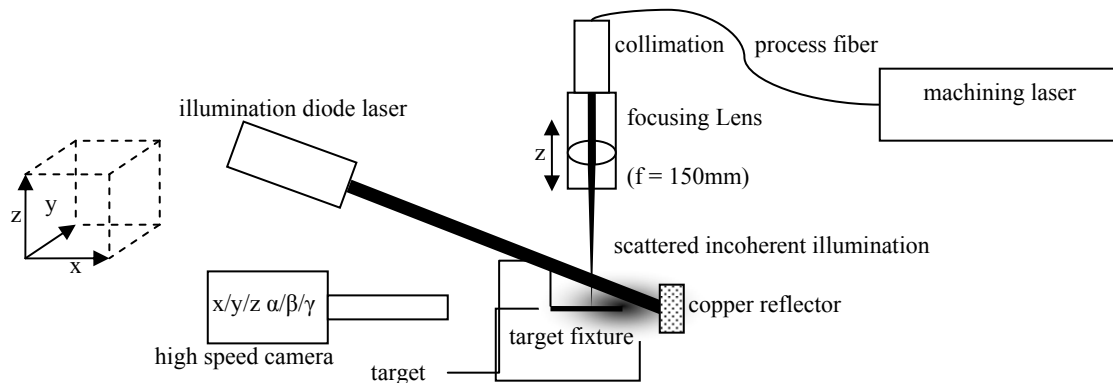


Figure 5: experimental setup of the high speed video recording.

$P_L$ [W]	$E_p$ [mJ]	PRR [kHz]	mode	feed rate [m/min]	focus diameter [ $\mu\text{m}$ ]	HSC recording speed [kfps]
6	0,3	20	T3	1	45	20

Table 5: Parameters of the laser cut for the high speed video recording.

## 2.4. Time resolved shadowgraph imaging.

To verify the hypothetical model of the ablation mechanism that was predicted based on the HSC recording and the calculation of the energy budget for a complete laser cut time resolved shadowgraph imaging (TRSI) was used. The principal setup of this experiment is shown in Figure 7. To avoid the necessity of a very precisely triggerable HSC and due to the fact that the measured jitter of the laser (i.e. time shift between gate signal from the signal control unit and the actual laser pulse) was longer than  $\pm 1\mu\text{s}$  a different strategy was used. A conventional CMOS camera was used in combination with a 1:1 telecentric lens. The source of illumination was a short pulsed, Q-switched rod type laser with a second harmonic generator to get an output wavelength of  $\lambda = 532\text{nm}$  at  $\tau = 3\text{ns}$  and  $E_p < 100\mu\text{J}$ . Due to the very short pulse duration of the green illumination laser the taken images show no visible motion blur even with an camera integration time of more than  $20\mu\text{s}$ . Figure 6 shows an example of a shadowgraph image taken with this technique.

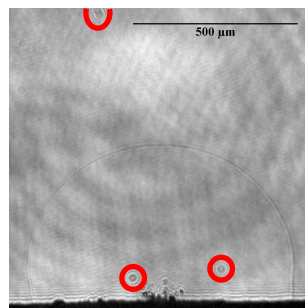


Figure 6: example of an anode image taken with 3ns of illumination time and 300ns after the laser pulse ( $\tau = 30\text{ns}$ ) impact.

The red marked circles indicate contamination of the camera optics which are not particles created by laser ablation of the anode coating. The next Figure 7 illustrates the setup of the TRSI. The two high speed diodes were used to determine the exact time difference between the ablation pulse and the illumination pulse and were set at the same distance from the target to ensure the same time of travel for both pulses. In order to shut off the IR radiation and most of the process scattering radiation a band pass filter with a central wave length (CWL) of 532nm was used. To get a representative result for each image the sample was manually moved with a precise linear stage to get a fresh sample surface for each pulse. The timing of the different signals (camera, ablation laser and illumination laser) was adjusted by a delay generator (DG353) and measured by the two high speed diodes and a digital oscilloscope (LeCroy Wave Runner 104Xi).

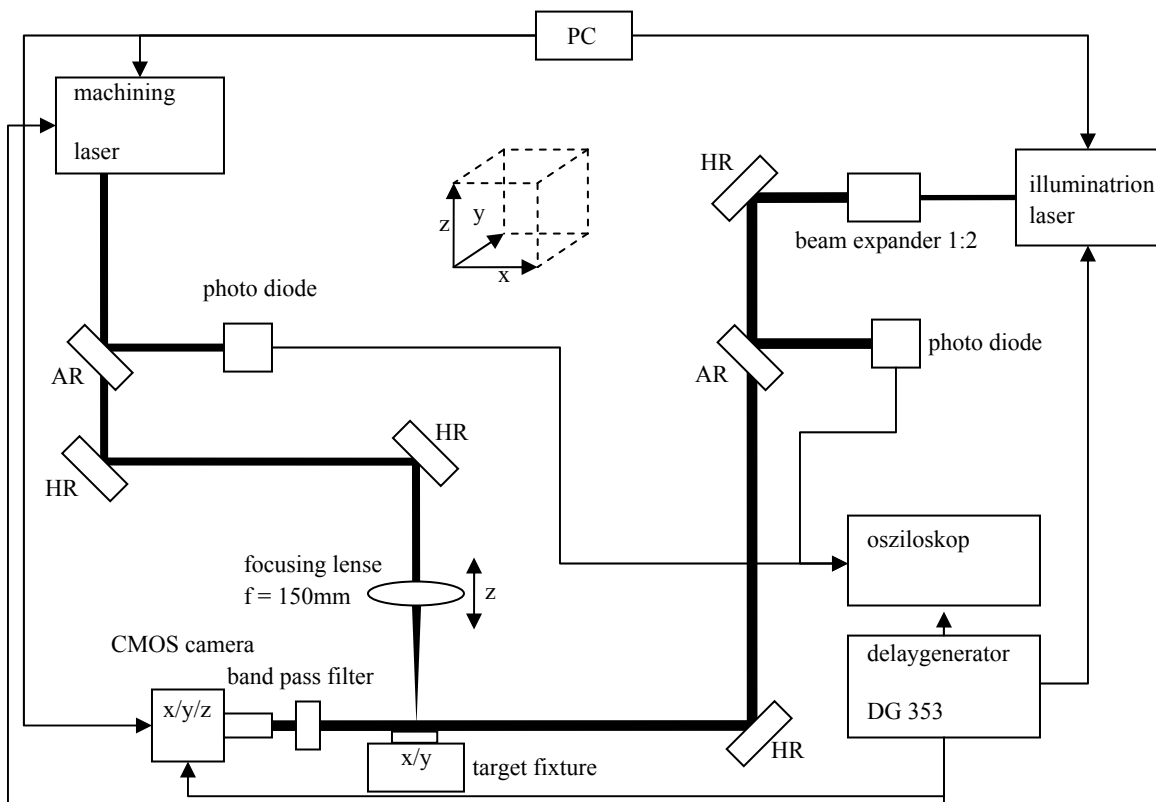


Figure 7: Setup of the time resolved shadowgraph imaging.

The timing of image taking is described in Figure 8. Due to the relatively long integration time and high jitter of multiple microseconds of the camera it was triggered primarily. Subsequently the ablation laser pulse was triggered and with the desired time delay the illumination pulse was applied.

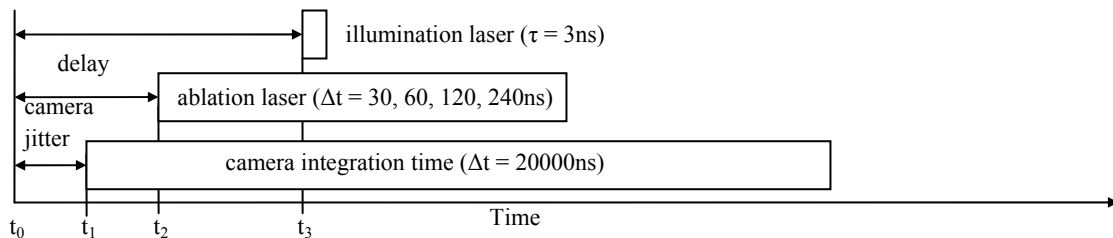


Figure 8: TRSG imaging timing.

The parameter groups used for this experiment are listed in Table 6. Besides the pulse energy  $E_p$  also the pulse duration  $\tau$  was varied to get a more universal statement about the validity of the hypothetical model.

Parameter group	$\tau$ [ns]	$E_p$ [mJ]	Focus diameter [ $\mu\text{m}$ ]
1	30	0,2	45
2	60	0,2	45
3	120	0,2	45
4	240	0,2	45
5	30	0,05	45
6	30	0,125	45
7	30	0,2	45

Table 6: Parameter groups used for the TRSG.

### 3. RESULTS AND DISCUSSION

#### 3.1. High speed video recording

In order to get a better impression of the results that were captured with HSC a stack of pictures was build. This was done by the image processing software ImageJ. The result can be seen in Figure 9. It represents a stack of one hundred consecutive frames from a high speed video taken at the parameters of Table 5.

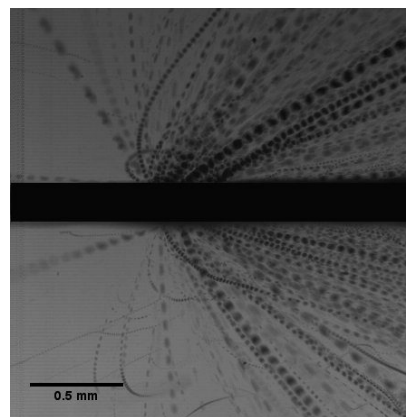


Figure 9: Stack of one hundred consecutive frames from the high speed video taken at the parameters of Table 5.

Figure 9 gives an insight into the mechanics of the laser cutting or the ablation process respectively. As it can be seen the most dominant process is not the evaporation of the coating but rather the ejection of complete coating particles. In order



to verify that assumption an energy budget calculation of the anode cutting has been done. This was done on the basis of a complete evaporation of graphite due to the lack of a melting of graphite under ambient atmosphere and evaporation of the CC without considering the melt-vapour-ratio of the CC ablation process. The ablated volumes removed by the laser cut were measured by an optical microscope. The results of this measurement (Figure 10) are listed in Table 7.

$b_{\Theta}$ [ $\mu\text{m}$ ]	$b_U$ [ $\mu\text{m}$ ]	$b_{CC}$ [ $\mu\text{m}$ ]	$h_O$ [ $\mu\text{m}$ ]	$h_U$ [ $\mu\text{m}$ ]	$h_{CC}$ [ $\mu\text{m}$ ]
165	128	28	61	61	11

Table 7: Measurement results of the laser cut performed for HSC video.

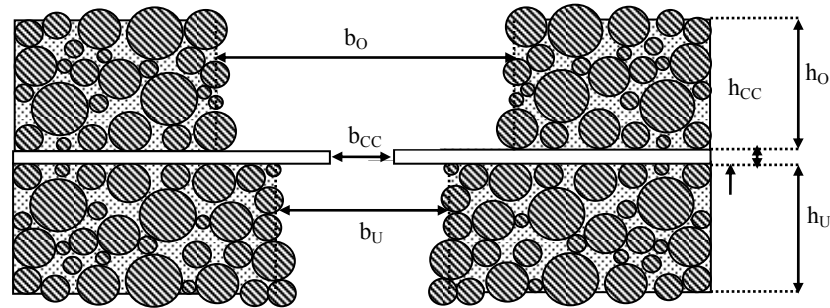


Figure 10: Measurements performed on the HSC video laser cut.

The energy budget was calculated with equations (3) and (4) based on the data from Table 2 and the assumption of complete absorption of the laser radiation.

$$E_{SubC} = E(T_0 - T_{Sub}) + \Delta H_{SubC} \quad (3)$$

$$E_{VCu} = E(T_0 - T_{FCu}) + \Delta H_{FCu} + E(T_{FCu} - T_{VCu}) + \Delta H_{VCu} \quad (4)$$

In equations (3) and (4)  $E_{SubC}$  is the sublimation energy for graphite, the ambient temperature  $T_0$  was set to 300K,  $T_{SubC}$  is the sublimation temperature of graphite and  $\Delta H_{SubC}$  the sublimation enthalpy of graphite.  $E_{VCu}$  denotes the energy that is necessary to evaporate the CC with the ambient temperature  $T_0$ , the temperature of fusion  $T_{FCu}$ , the boiling temperature  $T_{VCu}$  and the enthalpy of fusion  $\Delta H_{FCu}$  and evaporation  $\Delta H_{VCu}$ . The result is a total line energy  $E_{Line}$  of 2893J/m. Compared to that the actual line energy used for the full cut of only 353J/m was relatively small. This gap between theoretically calculated energy and the actual used  $E_{Line}$  indicates an ablation process that is not dominated by evaporation of the coating. Even when calculating the theoretical  $E_{Line}$  with the assumption of only melting the CC the theoretical  $E_{Line}$  only decreases by 10J/m. Based on the mismatch of the experimental and theoretical  $E_{Line}$  and the high speed video a hypothetical model of the ablation process was derived. It is established on the assumption that the coating particles are surrounded by the polymeric binder PVDF that has a relatively low evaporation point of about 660K with slight variations depending on the supplier. Figure 1 illustrates a single coating particle surrounded by PVDF. At  $t = t_0$  the laser hits the electrode surface and evaporates a thin layer of graphite. The amount of energy loss due to that evaporation is not considered in the calculation. Parts of this evaporated graphite later condense and form the so called Heat Affected Zone (HAZ). As the laser heats up the particle surface the heat diffuses through the particle and starts to heat up and evaporate the PVDF. As this heat front passes a critical point the created PVDF vapour starts to generate a

force that ejects the particle out of its compound. Depending on the material properties of the coating particles and the location of the critical point as well as the laser parameters, the time for the ejection  $t_{ejection}$  can be significantly longer than the pulse duration  $\tau$  itself. In this model the distance of this critical point from the highest point of particle was used as a fit factor and was set to the average particle size of  $10\mu\text{m}$ .

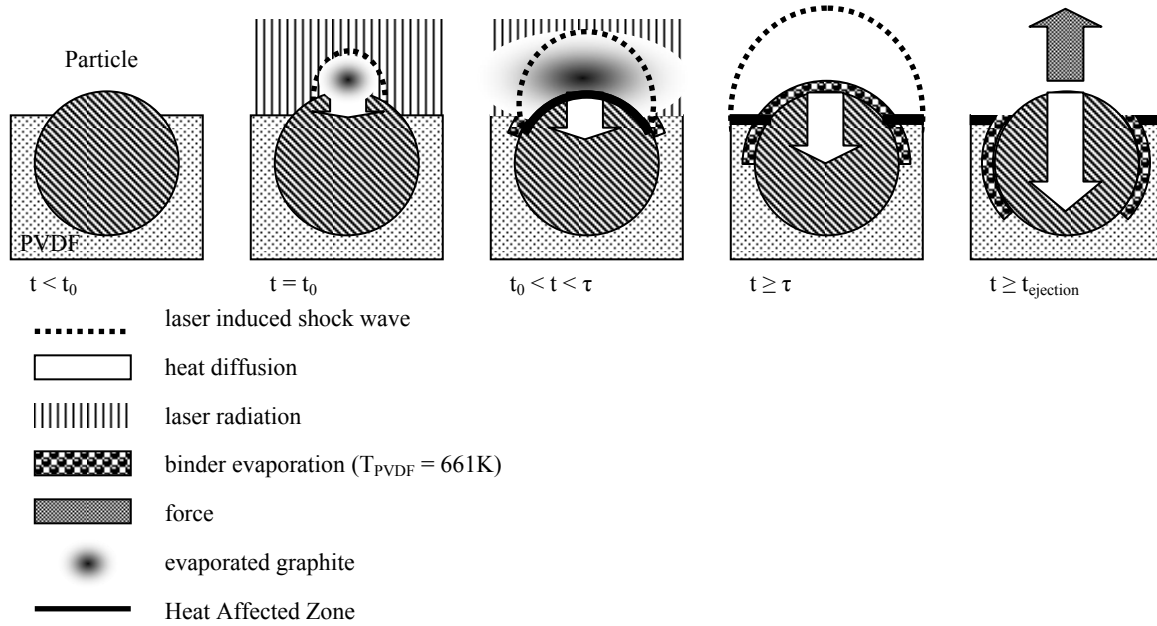


Figure 11: Illustration of the coating particle ablation process.

### 3.2. Time Resolved shadow graph

To verify the previously explained hypothetical model the theoretical time for ejection was calculated based on the material data from Table 2 and the equations (5)-(7) for the one dimensional heat diffusion induced by a locally infinite expanded heat input by a laser pulse with finite pulse duration [6].

$$T(z,t) = \frac{2I_L}{\rho c} \sqrt{\frac{t}{\kappa}} \text{ierfc}\left(\frac{z}{\sqrt{4\kappa t}}\right) + T_0 \quad (5)$$

$$\text{ierfc}(x) = \frac{1}{\sqrt{\pi}} e^{-x^2} \text{xerfc}(x) \quad (6)$$

$$T(z,t) = \frac{2I_L}{\rho c \sqrt{\kappa}} \left[ \sqrt{t} \text{erfc}\left(\frac{z}{\sqrt{4\kappa t}}\right) - \Theta(t-t_L) \sqrt{t-t_L} \text{ierfc}\left(\frac{z}{\sqrt{4\kappa(t-t_L)}}\right) \right] + T_0 \quad (7)$$

As the theoretical laser focus of  $45\mu\text{m}$  was large compared to the average particle size of  $10\mu\text{m}$  the calculation of the heat diffusion was done with a 1 dimensional model. Constant and homogenous intensity distributions on each particle surface as well as cubic shaped particles were assumed. The results of the calculation are illustrated in Figure 12

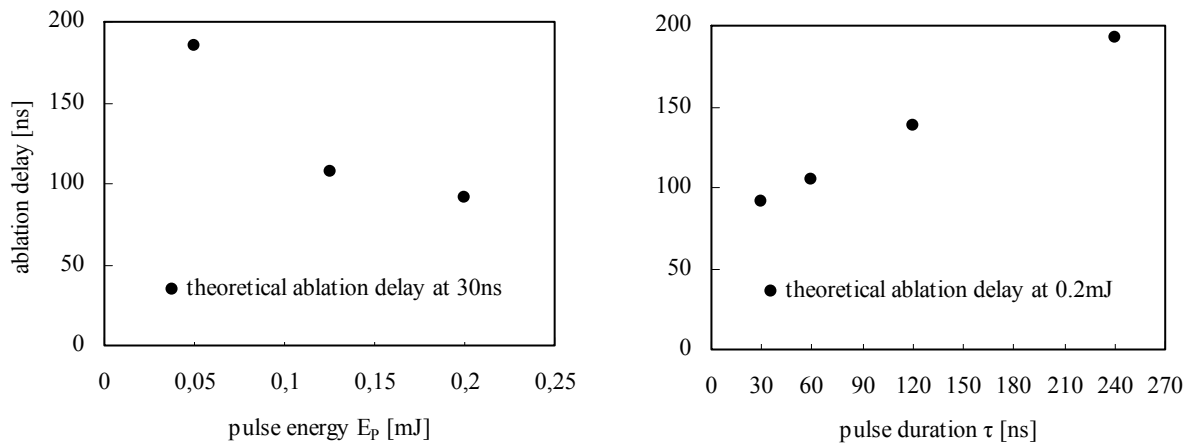


Figure 12: Calculated ablation delays for anode coating particles (left: depending on the pulse energy at  $\tau = 30\text{ns}$ ; right: depending on the pulse duration at  $E_p = 0.2\text{mJ}$ ).

It becomes clear that higher intensities caused by either higher pulse energies at constant pulse durations or shorter pulses at constant pulse energies cause a decrease of the ablation delay. Also the ablation delay can be significantly higher than the pulse duration itself which is, according to (7), caused by the speed of heat diffusion. To verify this data the chosen data points were evaluated experimentally. Figure 13 is an example of a time resolved shadow graphic picture sequence with selected frames that demonstrate the chronology of the ablation process at  $E_p = 0.2\text{mJ}$  and  $\tau = 30\text{ns}$ .

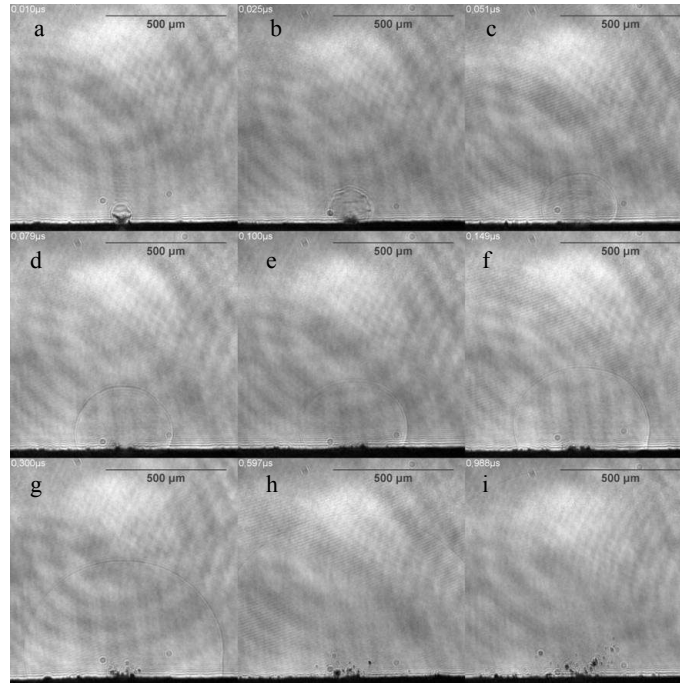


Figure 13: Picture sequence with selected frames at  $E_p = 0.2\text{mJ}$  and  $\tau = 30\text{ns}$ . The time delay of the illumination pulse relative to the machining laser pulse is written in the upper left corner of each frame.

The moment of ejection was determined by choosing the frame that showed the first particle ejections. In the example this was the picture taken at  $79 \pm 15\text{ns}$  after the impact of the machining laser pulse. To ensure the results, the following frames also had to show a clear ejection. All experiments were analyzed by the same procedure. The results are represented in Figure 14.

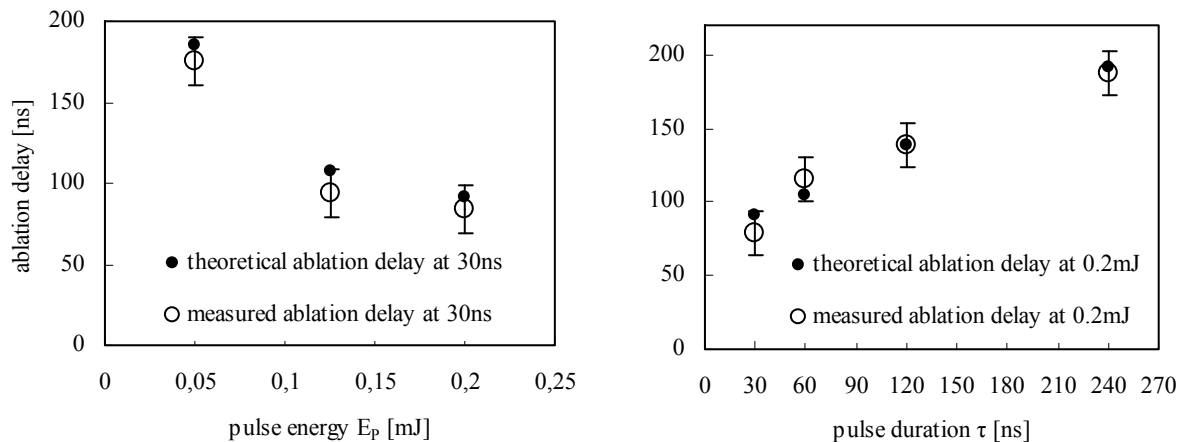


Figure 14: Comparison of measured and theoretical ablation delay for the parameters of Table 6. The error bars indicate the minimum temporal resolution of the time resolved shadow graphic imaging.

The error bars represent the temporal resolution of the experiment which was given by the frame rate and the systematic error of the illumination to laser pulse delay measurement measured by the digital oscilloscope. All calculated points lie within the max error of the measurement. In general a good qualitative and quantitative agreement

between the theoretical and the measured ablation delay can be observed which indicates a good validity of the hypothetical model

#### 4. SUMMARY AND CONCLUSION

By a simple tolerance stack up analysis of a half cell it could be revealed that there is a high need to systematically reduce the dead area of a Lithium Ion cell in order to increase the capacity without developing new active materials or cell designs. This goal can only be achieved by understanding the fundamentals of the laser cutting process and its phenomena like the clearance with, chamfer and delaminating of the active coating. The purpose of this study was to establish a theoretical ablation mechanism model of the Lithium Ion battery electrode coating and evaluate it by appropriate experimental methods. All experiments showed a good correlation with the theoretical result. Based on this model parameters like pulse duration, pulse energy as well as intensity distribution can be easily optimized to control the laser induced phenomena mentioned before without running extensive parameter studies. Further investigations will try to predict the ablation thresholds and the laser cutting edge phenomena by means of the theoretical ablation model and optimize the cutting parameters and intensity distribution with the goal to reduce the dead area.

#### REFERENCES

- [1] Agubra, V., Fergus, J., "Lithium Ion Battery Anode Aging Mechanism", Materials 2013 5, 1310-1325 (2013)
- [2] Luetke, M., Franke, V., Techel, A., Himmer, T., Klotzbach, U., Wetzig, A., Beyer, E., "A Comparative Study on Cutting Electrodes for Batteries with Lasers," Proc. Science Direct 12, 286-291 (2011).
- [3] Kornthaler, M., R., Schloegl, J., Kurfer, J., Wiedenmann, R., „Laser Cutting in the Production of Lithium Ion Cells“, Physics Procedia 39, 213-224 (2012)
- [4] Schmieder, B., "Laser cutting of graphite anodes for automotive lithium-ion secondary batteries: investigations in edge geometry and heat affected zone", Proc. SPIE 8244, laser-based Micro- and Nanopackaging and Assembly VI, 82440R (2012)
- [5] Lutey, A. H.A., Fortunato, A., Ascari, A., Carmignato, S., Leon, C., "Laser cutting of Lithium iron phosphate battery electrodes: Characterization of process efficiency and quality", Optics & Laser Technology 65, 164-174 (2015)
- [6] Poprawe, R., [Lasertechnik für die Fertigung], Springer-Verlag, Berlin Heidelberg 2005